International Forum on Aeroelasticity and Structural Dynamics
IFASD 2024
17-21 June 2024, The Hague, The Netherlands

DESIGN OF FLUTTER SUPPRESSION CONTROLLERS FOR A WING IN COMPRESSIBLE FLOW BASED ON HIGH-FIDELITY AERODYNAMICS

Boris Micheli, Jens Neumann, Jürgen Arnold[1]

[1]DLR - German Aerospace Center, Institute of Aeroelasticity
Bunsenstraße 10, 37073 Göttingen (DE)
boris.micheli@dlr.de
jens.neumann@dlr.de
juergen.arnold@dlr.de

Keywords: Aeroservoelasticity, active flutter suppression, compressible aerodynamics, CFD-CSM coupling, $\mathcal{H}_\infty$ control

Abstract: Since active flutter suppression technologies could lead to more efficient aircraft, they are acquiring increasingly importance and research activities relying on wind tunnel demonstrators are flourishing to gain experience and knowledge. Aeroelastic models employed for control activities are traditionally based on Generalized Aerodynamic Forces (GAFs) computed through DLM in reduced frequency domain. The main limitation of this approach is that compressible flow exhibits nonlinearities which are not captured by DLM. To overcome this shortcoming, this paper solves the governing equations of motion in time domain coupling a structural dynamic solver and CFD Euler aerodynamics. The aeroelastic system is excited to identify the CFD GAFs which are coupled with the structural matrices yielding a more accurate state space realization of the aeroelastic system suited for control design activities. The state space realizations are then exploited to design $\mathcal{H}_\infty$-based flutter suppression controllers, which are implemented in the fully coupled computational fluid/structural dynamics solver to demonstrate the damping augmentation capabilities of the compensators. The approach is demonstrated on a realistic aeroelastic system and comprehensive nonlinear computations using controllers synthesized based on GAFs either computed via Euler CFD or uncorrected DLM are presented. Differences in the results, even at subsonic Mach numbers, will be explained based on comparative analyses of the different pressure fields, highlighting the benefits of using high-fidelity aerodynamics.

1 INTRODUCTION

Aeroelastic flutter is a type of instability that involves the adverse interaction of unsteady aerodynamics with structural dynamics and produces an unstable oscillation that often results in structural failure [1]. Conventional aircraft are designed in compliance with the Federal Aviation Administration (FAA) [2] and the European Aviation Safety Agency (EASA) certification specification 25.629 [3] such that flutter does not occur within the range of their operating conditions. A comprehensive overview on active flutter suppression (AFS) activities is provided in [4].

To date, the majority of the experimental activities that successfully demonstrated flutter suppression relied on classic or robust control methodologies which require the equations of motion

(EOMs) of the aeroelastic plant to be cast in a linear time-invariant (LTI) state space form. State space realizations are derived either from theoretical principles or numerically via Finite Element (FE) models coupled with vortex-lattice method (VLM)\doublet-lattice method (DLM) aerodynamics [5, 6]. The former modelling approach was employed by Schildkamp et al. [7] to demonstrate AFS on a wing apparatus that resembles the two-dimensional wing section of Theodorsen [1], as well as within the NASA Benchmark Active Controls Technology (BACT) program [8–10]. In this program, the EOMs describing the dynamics of a rigid rectangular straight wing, capable of plunging and pitching, were refined by substituting the unsteady aerodynamic coefficients with their identified values. This refinement aimed to better capture the aeroelastic behavior in the transonic regime.

When dealing with more elaborate configurations such as Unmanned Aerial Vehicles (UAVs) or complete aircraft wind tunnel models, the modelling approach based on FE models and DLM aerodynamics stands out as the most convenient option. This approach paved the way for the synthesis of a large variety of flutter suppression controllers within the experimental campaigns carried out on the X-DIA and F-XDIA models in Politecnico di Milano within the last 15 years [11–14]. In-flight demonstrations of AFS that relied on a similar modelling approach for the synthesis of the compensator are the activities carried out on the X-56A research vehicle developed in a joint effort between NASA centers and Boeing [15, 16], and in the context of the European FlexOp [17] and FliPASED[1] projects.

The common denominator of the above mentioned demonstrators is that they are immerse in subsonic incompressible flow, whose dynamics is properly captured by potential solvers such as DLM that is the state-of-the-art method used for predicting unsteady airloads. It is based on potential theory for thin wing geometry. Therefore, it cannot account for the wing thickness or capture recompression shocks and boundary layer separation. To overcome these limitations typical of the transonic regime, DLM corrections based on wind tunnel data or computational methods of higher fidelity can be employed. Flutter suppression controllers derived from higher fidelity aerodynamics have been synthesized in multiple numerical investigations [18, 19]. Particularly relevant is the work carried out by Weite et el. [20], where Reynolds-averaged Navier-Stokes (RANS) equations were simulated to train reduced-order models (ROMs) to be used for control synthesis. The synthesized controllers are afterwards tied to the RANS solver to demonstrate AFS within a computational aeroservoelastic (ASE) model that uses a nonlinear aerodynamic solver on a realistic airplane configuration. However, these endeavors remained limited to numerical investigations. Since wind tunnel experiments focusing on AFS at high Mach numbers are thriving (e.g. the American sub-project IAWTM [21] and DLR project ACTIVATE), the development of generalizable ASE modelling and analyses methodologies to support testing in compressible flows assumes a key role.

The goal of this work is to demonstrate a workflow ranging from the generation of ASE state space realizations based on computational fluid dynamics (CFD) data up to AFS controller synthesis, and post-synthesis verification of the closed-loop (CL) performance in a nonlinear simulation framework. The simulation environment utilized in this study is PyCSM, a software developed by Neumann [22] that solves the EOMs in time domain by embedding the DLR TAU-Code [23] for the prediction of unsteady airloads and by carrying out all the necessary CFD-Computational Structural Mechanics (CFD-CSM) couplings. PyCSM is further enhanced with a mesh deformation module to permit control surface deflections, along with a simplified actuator dynamics that includes amplitude and rate saturation as elaborated in [24].

[1] https://www.dlr.de/en/latest/news/2023/03/scientists-tame-dreaded-aviation-phenomenon

The enhanced software is named PyCSM-ASE. To demonstrate the feasibility of the proposed workflow and the capabilities of PyCSM-ASE, the application of the TAU-Code is restricted to solving Euler aerodynamics. This decision is made to circumvent complexities associated with selecting turbulence models and defining boundary layers.

The structure of the manuscript reflects the steps of the proposed workflow. The theoretical principles for the linearization of the generalized aerodynamic forces (GAFs) and the generation of ASE state space realizations based on CFD data are discussed in Section 2. Section 3 formulates the control objective pursued in this study and details the structure of the controller utilized to address it. An overview of the process flow of PyCSM-ASE is elucidated in Section 4. Numerical investigations are conducted replicating the characteristics of the BACT wind-tunnel model which is representative of a generic aeroelastic plant. Its geometry is described in Section 5, which also encompasses comparisons between state space realizations generated via Euler CFD and those obtained through uncorrected DLM at varying Mach numbers, alongside numerical results derived from nonlinear simulations in PyCSM-ASE. Concluding remarks are provided in Section 6.

2 AEROSERVOELASTIC MODELLING

The nonlinear time EOMs that describe the dynamics of a flexible aircraft expressed in its modal coordinates read

$$\mathbf{M}_{\text{hh}}\ddot{\mathbf{u}}_{\text{h}}(t)+\mathbf{B}_{\text{hh}}\dot{\mathbf{u}}_{\text{h}}(t)+\mathbf{K}_{\text{hh}}\mathbf{u}_{\text{h}}(t)+\mathbf{M}_{\text{hc}}\ddot{\boldsymbol{\delta}}(t)=\underbrace{\boldsymbol{\phi}_{\text{gh}}^{T}\boldsymbol{\phi}_{\text{jg}}^{T}\mathbf{f}_{\text{j}}(t,\mathbf{u}_h,\dot{\mathbf{u}}_h,\ddot{\mathbf{u}}_h,\boldsymbol{\delta},\dot{\boldsymbol{\delta}},\ddot{\boldsymbol{\delta}},\mathbf{w}_{\text{g}},\mathbf{p},\text{geometry})}_{\mathbf{f}_{\text{h}}(t,\mathbf{u}_h,\dot{\mathbf{u}}_h,\ddot{\mathbf{u}}_h,\boldsymbol{\delta},\dot{\boldsymbol{\delta}},\ddot{\boldsymbol{\delta}},\mathbf{w}_{\text{g}},\mathbf{p},\text{geometry})} \tag{1}$$

where $\mathbf{K}_{\text{hh}}$, $\mathbf{C}_{\text{hh}}$, and $\mathbf{M}_{\text{hh}}$ denotes the generalized stiffness, damping and mass matrices respectively, $\mathbf{M}_{\text{hc}}$ is the generalized coupling mass matrix which enables to account for the inertial forces due to a control surface deflection, $\mathbf{u}_{\text{h}}$, $\dot{\mathbf{u}}_{\text{h}}$, and $\ddot{\mathbf{u}}_{\text{h}}$ ($\boldsymbol{\delta}$, $\dot{\boldsymbol{\delta}}$, and $\ddot{\boldsymbol{\delta}}$) are the generalized coordinates (control surface deflections) and related derivatives. The vector $\mathbf{f}_{\text{j}}(\cdot)$ describes the aerodynamic forces which are computed at the aerodynamic degrees-of-freedom (DOFs) defined either by the corner of the CFD mesh that models the wet surface of the configuration or the $3/4$ points of the DLM panels. This set of DOFs is denoted as the j-set. The projection of $\mathbf{f}_{\text{j}}(\cdot)$ on the modal DOFs, i.e. the h-set, yields the modal aerodynamic forces $\mathbf{f}_{\text{h}}(\cdot)$. The projection is accomplished by means of the matrix of eigenvalues $\boldsymbol{\phi}_{\text{gh}}$ and the CFD-CSM coupling matrix $\boldsymbol{\phi}_{\text{jg}}$ which is necessary to transfer the displacements from the structural DOFs defined by the FE model, i.e. the g-set, to the aerodynamic DOFs according to $\mathbf{u}_{\text{j}}(t)=\boldsymbol{\phi}_{\text{jg}}\mathbf{u}_g(t)$[2]. The vectors $\mathbf{w}_{\text{g}}$ and $\mathbf{p}$ serve to describe the dependency of the aerodynamic forces from the wind speed, namely perturbations of the steady flow, and the parameters that describe the flow conditions, e.g. asymptotic Mach number M_∞, dynamic pressure q_∞, fluid viscosity μ_∞, Reynolds number Re, etc.

In Eq. (1) the nonlinearity originates from the non homogenous term, as the unsteady aerodynamic forces $\mathbf{f}_{\text{j}}(\cdot)$ are in general a nonlinear function of the various parameters. Equation (1) is further augmented with the actuators dynamics which is described by a set of differential equations of the form

$$\{\boldsymbol{\delta},\dot{\boldsymbol{\delta}},\ddot{\boldsymbol{\delta}}\}=\mathbf{f}_{\text{act}}(t,\boldsymbol{\delta}_c) \tag{2}$$

[2]Based on the principle of virtual work one can show that also the forces are transferred through the coupling matrix according to $\mathbf{f}_{\text{g}}(\cdot)=\boldsymbol{\phi}_{\text{jg}}^{T}\mathbf{f}_{\text{j}}(\cdot)$

where $\mathbf{f}_{\text{act}}(\cdot)$ denotes a nonlinear set of functions which depends on the specific actuator dynamics as well as on its kinematic chain, whereas $\boldsymbol{\delta}_c$ is the vector of commanded control surface deflections. Common nonlinearities which are modelled by $\mathbf{f}_{\text{act}}(\cdot)$ and have an influence on the overall ASE performance comprise backlash, free play, or rate and deflection limits [24]. Generally, an additional set of differential equations which describes the sensor dynamics is also added. This set of equations reads

$$\mathbf{y} = \mathbf{f}_{\text{sens}}(t, \mathbf{u}_h, \dot{\mathbf{u}}_h, \ddot{\mathbf{u}}_h, \boldsymbol{\delta}, \dot{\boldsymbol{\delta}}, \ddot{\boldsymbol{\delta}}, \mathbf{p}, \mathbf{w}_g) \tag{3}$$

where the dependency on $\mathbf{p}$ is necessary to model pressure transducers and $\mathbf{w}_g$ is necessary for the numerical modelling of lidar-based sensors. Finally, sensor measurements are elaborated by the specific controller $\hat{\mathbf{f}}(\cdot)$ which provides the new commanded deflection to be delivered to the actuators to achieve the specific control target, namely

$$\boldsymbol{\delta}_c = \hat{\mathbf{f}}(t, \mathbf{y}, \boldsymbol{\delta}_{\text{track}}) \tag{4}$$

where $\boldsymbol{\delta}_{\text{track}}$ describes the pilot command to be tracked. The connection of Eqs. (1), (2), (3), and (4) provides the most general description of an ASE system and they are solved through PyCSM-ASE as detailed in Section 4. Figure 1 provides an illustration of the interconnection between these equations.

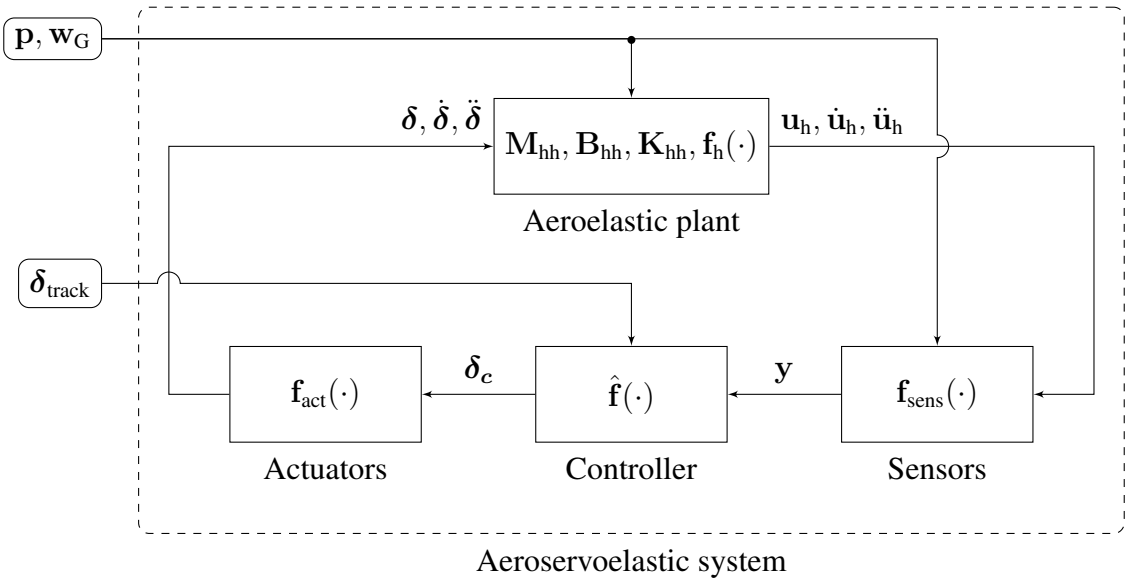

Figure 1: Schematic interconnection of equations.

2.1 Linearization of Unsteady Aerodynamic Forces

To be suitable for control activities, Eq. (1), (2), and (3) must be formulated in a LTI form. Whereas linear identification techniques for the characterization of $\mathbf{f}_{\text{act}}(\cdot)$ and $\mathbf{f}_{\text{sens}}(\cdot)$ are broadly employed, the linearization of the term $\mathbf{f}_{\text{h}}(\cdot)$ that describes the unsteady aerodynamic flow over the aeroelastic configuration represents a main hurdle. Typically, $\mathbf{f}_{\text{h}}(\cdot)$ is characterized by means of its frequency response which is computed running forced motion simulations using harmonic excitations for the mode shapes or control surfaces of interest. In subsonic flows this is carried out through DLM that is founded on linear potential theory. Based on the linearity of the method, the superposition principle is applied to split the unsteady aerodynamic forces into their basic contributions as

$$\mathbf{f}_{\text{h}}(\cdot) = \mathbf{f}_{\text{h}}^{\text{aero}}(t, \mathbf{u}_h, \dot{\mathbf{u}}_h, \ddot{\mathbf{u}}_h, \mathbf{p}, \text{geom.}) + \mathbf{f}_{\text{h}}^{\text{cs}}(t, \boldsymbol{\delta}, \dot{\boldsymbol{\delta}}, \ddot{\boldsymbol{\delta}}, \mathbf{p}, \text{geom.}) + \mathbf{f}_{\text{h}}^{\text{ext}}(t, \mathbf{w}_{\text{g}}, \mathbf{p}, \text{geom.}) \tag{5}$$

where $\mathbf{f}_{\text{h}}^{\text{aero}}(\cdot)$, $\mathbf{f}_{\text{h}}^{\text{cs}}(\cdot)$, and $\mathbf{f}_{\text{h}}^{\text{ext}}(\cdot)$ are the time dependent aerodynamic forces due to structural modes, control surface deflections and atmospheric perturbations, respectively. The frequency responses are then approximated as

$$\begin{aligned}
\mathbf{f}_{\text{h}}^{\text{aero}}(ik, M_\infty, q_\infty) &= q_\infty \mathbf{Q}_{\text{hh}}^{\text{DLM}}(ik, M_\infty)\mathbf{u}_h(ik) \\
\mathbf{f}_{\text{h}}^{\text{cs}}(ik, M_\infty, q_\infty) &= q_\infty \mathbf{Q}_{\text{hc}}^{\text{DLM}}(ik, M_\infty)\boldsymbol{\delta}(ik) \\
\mathbf{f}_{\text{h}}^{\text{ext}}(ik, M_\infty, q_\infty) &= q_\infty \mathbf{Q}_{\text{hg}}^{\text{DLM}}(ik, M_\infty)\mathbf{w}_g(ik)
\end{aligned} \tag{6}$$

where k is the reduced frequency, $\mathbf{Q}_{\text{hh}}^{\text{DLM}}$, $\mathbf{Q}_{\text{hc}}^{\text{DLM}}$, and $\mathbf{Q}_{\text{hg}}^{\text{DLM}}$ are the generalization of $\mathbf{f}_{\text{h}}^{\text{aero}}(\cdot)$, $\mathbf{f}_{\text{h}}^{\text{cs}}(\cdot)$, and $\mathbf{f}_{\text{h}}^{\text{ext}}(\cdot)$ respectively, i.e. the so-called Generalized Aerodynamic Forces (GAFs). In the DLM framework the dependency of $\mathbf{f}_{\text{h}}^{\text{aero}}(\cdot)$, $\mathbf{f}_{\text{h}}^{\text{cs}}(\cdot)$, and $\mathbf{f}_{\text{h}}^{\text{ext}}(\cdot)$ from $\mathbf{p}$ boils down to the asymptotic Mach number M_∞ and dynamic pressure q_∞. Since DLM describes an inviscid and irrotational flow, phenomena such as shock effects and boundary layer separations are not accounted. Effects of lifting surfaces thickness are also not captured, whereas twist and camber characteristics can be modelled correcting the direction of the normal vectors of the panels. However, these corrections are reliable only for limited degrees of twist and camber, hence being unsuitable for accurately modeling highly curved or intricate geometries. Despite that, DLM is state-of-the-art for the linearization of unsteady aerodynamic loads in industrial aeroelastic analyses and it is here employed as a reference. Specifically, the DLM formulation employed in this manuscript is the one from the aeroelastic software package ZAERO [25].

To enhance the accuracy of GAFs computations, this work proposes to run forced motion simulations in the time domain within a CFD framework that solves Euler equations. The aerodynamic frequency response can then be calculated assessing the frequency content of the time domain forces through a Fast Fourier Transform (FFT) algorithm. To generalize $\mathbf{f}_{\text{h}}$ in a form consistent with Eq. (5), the modes of the system, as well as the control surfaces, are excited via mesh deformation with a pulse excitation of the form

$$\begin{aligned}
\mathbf{u}_{\text{h}_i}(t) &= \begin{cases} 4 \cdot u_i \left(\frac{t}{t_0}\right)^2 e^{\left(2 - \frac{1}{1-\frac{t}{t_0}}\right)} & \text{if} \quad 0 \leq t < t_0 \\ 0 \quad \text{if} \quad t \geq t_0 \end{cases} \\
\boldsymbol{\delta}_i(t) &= \begin{cases} 4 \cdot \delta_i \left(\frac{t}{t_0}\right)^2 e^{\left(2 - \frac{1}{1-\frac{t}{t_0}}\right)} & \text{if} \quad 0 \leq t < t_0 \\ 0 \quad \text{if} \quad t \geq t_0 \end{cases}
\end{aligned} \tag{7}$$

where u_i and δ_i define the amplitude of the excitation and t_0 the duration of the signal correlated to its frequency content. Lower values of t_0 lead to broader frequency spectra. Since most of the aeroelastic phenomena of interest are happening at low frequencies, the value of t_0 is adjusted depending on the flow conditions to achieve an excitation with a spectrum that has 98% of its content below $k = 2.0$. The values of the Euler-based GAFs $\mathbf{Q}_{\text{hh}}^{\text{Eul}}$ and $\mathbf{Q}_{\text{hc}}^{\text{Eul}}$ are computed column by column as

$$\begin{aligned}
\mathbf{Q}_{\text{hh}}^{\text{Eul}}[:, i] &= \frac{\text{fft}\left[\left(\mathbf{f}_h(t, \dots) - \mathbf{f}_{\text{steady}}\right)/q_\infty\right]}{\text{fft}(\mathbf{u}_{\text{h}_i(t)})} \\
\mathbf{Q}_{\text{hc}}^{\text{Eul}}[:, i] &= \frac{\text{fft}\left[\left(\mathbf{f}_h(t, \dots) - \mathbf{f}_{\text{steady}}\right)/q_\infty\right]}{\text{fft}(\boldsymbol{\delta}_i(t))}
\end{aligned} \tag{8}$$

where $\mathbf{Q}_{\text{hh}}^{\text{Eul}}[:, i]$ ($\mathbf{Q}_{\text{hc}}^{\text{Eul}}[:, i]$) denotes the i^{th} column of $\mathbf{Q}_{\text{hh}}^{\text{Eul}}$ ($\mathbf{Q}_{\text{hc}}^{\text{Eul}}$) and $\mathbf{f}_{\text{steady}}$ is the converged state of a precomputed static aeroelastic simulation. The so-computed GAFs are able to

capture compressibility and general complex geometries, namely

$$\begin{aligned}\mathbf{Q}_{\text{hh}}{}^{\text{Eul}} &= \mathbf{Q}_{\text{hh}}{}^{\text{Eul}}(ik, M_\infty, \rho_\infty, \text{geometry}) \\ \mathbf{Q}_{\text{hc}}{}^{\text{Eul}} &= \mathbf{Q}_{\text{hc}}{}^{\text{Eul}}(ik, M_\infty, \rho_\infty, \text{geometry})\end{aligned} \tag{9}$$

The main steps for the computation of $\mathbf{Q}_{\text{hh}}{}^{\text{Eul}}$ and $\mathbf{Q}_{\text{hc}}{}^{\text{Eul}}$ are summarized in Algorithm 1. The computation of the frequency response $\mathbf{f}_{\text{h}}{}^{\text{ext}}(ik)$ that appears in Eq. (6) can be accomplished adopting the methodologies presented by Kaiser et al. [26]. However, this manuscript introduces the excitation term as a direct time excitation $\mathbf{f}_{\text{h}}{}^{\text{ext}}(t)$ in accordance with Eq. (5) to facilitate the comparison of the DLM and CFD performance in CL during the nonlinear simulation assessments.

Algorithm 1 Computation of GAFs based on iterative CFD-CSM simulations.

Inputs:

- Generalized structural stiffness $\mathbf{K}_{\text{hh}}$, damping $\mathbf{B}_{\text{hh}}$, and mass matrices $\mathbf{M}_{\text{hh}}$
- Matrix of structural eigenvectors $\boldsymbol{\phi}_{gh}$ and FE model geometry $\mathbf{x}_g$
- CFD mesh and coordinate of the wet surface $\mathbf{x}_j$
- Vector of parameters with simulated flow conditions $\mathbf{p}$
- Amplitude of modal displacements $\mathbf{u}_i$ and control surface deflection $\boldsymbol{\delta}_i$

Outputs:

- Euler-based GAFs $Q_{\text{hh}}{}^{\text{Eul}}(ik, M_\infty, \rho_\infty, \text{geometry})$ and $Q_{\text{hc}}{}^{\text{Eul}}(ik, M_\infty, \rho_\infty, \text{geometry})$

Body algorithm:

1. *Splining:* Computation of the CFD-CSM coupling matrix $\boldsymbol{\phi}_{jh}$ through the so-called scattered data interpolation methods based on radial basis functions as proposed by Beckert and Wendland [27]. Based on the interpolation approach, $\mathbf{u}_j = \boldsymbol{\phi}_{jg}\mathbf{u}_g$ and $\mathbf{f}_g = \boldsymbol{\phi}_{jg}^T\mathbf{f}_j$.
2. *Trim:* Computation of the trim state $\mathbf{f}_{\text{steady}}$ for the set of simulation parameters $\mathbf{p}$ by means of the iterative algorithms presented by Farhat and Lesoinne [28].
3. *Unsteady CFD-CSM simulations and GAFs identification:*
   for $i := 1 : n_{\text{h}}$
   - ➢ Impose $\mathbf{u}_{\text{u}_i}$ ($\boldsymbol{\delta}_i$) according to Eq. 7.
   - ➢ Solve for $\mathbf{f}_{\text{h}}(t)$ in Eq. 1 through the iterative CFD-CSM procedure [22].
   - ➢ Computation of $\mathbf{Q}_{\text{hh}_i}{}^{\text{Eul}}$ ($\mathbf{Q}_{\text{hc}_i}{}^{\text{Eul}}$) according to Eq. 8.

   end for

   where n_{h} is the number of modes.

2.2 Linear Models for Control Activities

Regardless of whether the DLM or the proposed CFD-based procedure is employed, the aerodynamic models describing the flow over the aircraft are provided within the frequency domain in tabular form and cannot be arranged in a LTI state space form by a direct application of the inverse Laplace transform. In this manuscript, the LTI representation is accomplished through vector fitting routines [29–31] which are applied to the GAFs computed in reduced frequency domain yielding

$$\mathbf{Q}(\overline{s}) = \left[\mathbf{Q}_{\text{hh}}(\overline{s}), \mathbf{Q}_{\text{hc}}(\overline{s})\right] \approx \mathbf{C}\left(\overline{s}\mathbf{I} - \mathbf{A}\right)^{-1}\mathbf{B} + \mathbf{D} + \overline{s}\mathbf{E} \tag{10}$$

where $\overline{s}$ is the reduced Laplace variable computed as $\overline{s} = sL/V_\infty$ consistently with the definition of k. L represents a reference length of the aeroelastic system and V_∞ the asymptotic true-airspeed. The explicit state space realization that describes the input-output relationship between

$\mathbf{f}_{\text{h}}(\cdot)$ and $\left\{\mathbf{u}_{\text{h}}, \dot{\mathbf{u}}_{\text{h}}, \boldsymbol{\delta}, \dot{\boldsymbol{\delta}}, \mathbf{f}_{\text{h}}{}^{\text{ext}}(t)\right\}$ is derived from Eqs. (5) and (10) yielding

$$\begin{aligned}\dot{\boldsymbol{\xi}}_{\text{a}}(t) &= \underbrace{(V_\infty/L)\mathbf{A}}_{\mathbf{A}_a}\boldsymbol{\xi}_{\text{a}}(t) + \underbrace{(V_\infty/L)\mathbf{B}}_{\mathbf{B}_a}\left\{\mathbf{u}_{\text{h}}(t), \boldsymbol{\delta}_{\text{c}}(t)\right\} \\ \mathbf{f}_{\text{h}}(t) &= \underbrace{q_\infty\mathbf{C}}_{\mathbf{C}_a}\boldsymbol{\xi}_{\text{a}}(t) + \underbrace{q_\infty\mathbf{D}}_{\mathbf{D}_a}\left\{\mathbf{u}_{\text{h}}(t), \boldsymbol{\delta}_{\text{c}}(t)\right\} + \underbrace{q_\infty(L/V_\infty)\mathbf{E}}_{\mathbf{E}_a}\left\{\dot{\mathbf{u}}_{\text{h}}(t), \dot{\boldsymbol{\delta}}(t)\right\} + \mathbf{f}_{\text{h}}{}^{\text{ext}}(t)\end{aligned} \tag{11}$$

where $\boldsymbol{\xi}_{\text{a}}(t)$ are the aerodynamic lag states that model the aerodynamic lag effects due to the unsteadiness of the flow and matrix $\mathbf{B}_a$ is partitioned as $\mathbf{B}_a = [\mathbf{B}_{\text{h}}, \mathbf{B}_{\text{cs}}]$ likewise $\mathbf{D}_a$ and $\mathbf{E}_a$. The realization defined by Eq. (11) is included in Eq. (1) to provide the state space model of the aeroelastic system $\mathcal{S}_{\text{ae}}$. Explicitly

$$\begin{aligned}\begin{Bmatrix}\dot{\mathbf{u}}_{\text{h}}(t)\\ \ddot{\mathbf{u}}_{\text{h}}(t)\\ \dot{\boldsymbol{\xi}}_{\text{a}}(t)\end{Bmatrix} &= \underbrace{\begin{bmatrix}\mathbf{0} & \mathbf{I} & \mathbf{0}\\ -\mathbf{M}_{\text{hh}}^{-1}\mathbf{K}_{\text{eq}} & -\mathbf{M}_{\text{hh}}^{-1}\mathbf{B}_{\text{eq}} & \mathbf{M}_{\text{hh}}\mathbf{C}_{\text{a}}\\ \mathbf{B}_{\text{h}} & \mathbf{0} & \mathbf{A}_{\text{a}}\end{bmatrix}}_{\mathbf{A}_{\text{ae}}}\begin{Bmatrix}\mathbf{u}_{\text{h}}(t)\\ \dot{\mathbf{u}}_{\text{h}}(t)\\ \boldsymbol{\xi}_{\text{a}}(t)\end{Bmatrix} + \dots \\ &\quad \dots \underbrace{\begin{bmatrix}\mathbf{0} & \mathbf{0} & \mathbf{0} & \mathbf{0}\\ \mathbf{M}_{\text{hh}}^{-1}\mathbf{D}_{\text{cs}} & \mathbf{M}_{\text{hh}}^{-1}\mathbf{E}_{\text{cs}} & -\mathbf{M}_{\text{hh}}\mathbf{M}_{\text{hc}} & \mathbf{M}_{\text{hh}}^{-1}\mathbf{I}\\ \mathbf{B}_{\text{cs}} & \mathbf{0} & \mathbf{0} & \mathbf{0}\end{bmatrix}}_{\mathbf{B}_{\text{ae}}}\begin{Bmatrix}\boldsymbol{\delta}(t)\\ \dot{\boldsymbol{\delta}}(t)\\ \ddot{\boldsymbol{\delta}}(t)\\ \mathbf{f}_{\text{h}}(t)\end{Bmatrix}\end{aligned} \tag{12}$$

$$\begin{Bmatrix}\mathbf{u}_{\text{h}}(t)\\ \dot{\mathbf{u}}_{\text{h}}(t)\\ \ddot{\mathbf{u}}_{\text{h}}(t)\end{Bmatrix} = \underbrace{\begin{bmatrix}\begin{bmatrix}\mathbf{I} & \mathbf{0} & \mathbf{0}\end{bmatrix}\mathbf{I}\\ \begin{bmatrix}\mathbf{I} & \mathbf{0} & \mathbf{0}\end{bmatrix}\mathbf{A}_{\text{ae}}\\ \begin{bmatrix}\mathbf{I} & \mathbf{0} & \mathbf{0}\end{bmatrix}\mathbf{A}_{\text{ae}}^2\end{bmatrix}}_{\mathbf{C}_{\text{ae}}}\begin{Bmatrix}\mathbf{u}_{\text{h}}(t)\\ \dot{\mathbf{u}}_{\text{h}}(t)\\ \boldsymbol{\xi}_{\text{a}}(t)\end{Bmatrix} + \underbrace{\begin{bmatrix}\mathbf{0}\\ \mathbf{0}\\ \begin{bmatrix}\mathbf{I} & \mathbf{0} & \mathbf{0}\end{bmatrix}\mathbf{A}_{\text{ae}}\mathbf{B}_{\text{ae}}\end{bmatrix}}_{\mathbf{D}_{\text{ae}}}\begin{Bmatrix}\boldsymbol{\delta}(t)\\ \dot{\boldsymbol{\delta}}(t)\\ \ddot{\boldsymbol{\delta}}(t)\\ \mathbf{f}_{\text{h}}(t)\end{Bmatrix}$$

where $\mathbf{K}_{\text{eq}} = \mathbf{K}_{\text{hh}} - \mathbf{D}_{\text{h}}$ and $\mathbf{B}_{\text{eq}} = \mathbf{B}_{\text{hh}} - \mathbf{E}_{\text{h}}$. Finally, Eq. (12) is concatenated with the actuator dynamics which is identified from Eq. (2) as $\mathcal{S}_{\text{act}} = [\mathbf{A}_{\text{act}}, \mathbf{B}_{\text{act}}, \mathbf{C}_{\text{act}}, \mathbf{D}_{\text{act}}]$ and the linearized sensors dynamics $\mathcal{S}_{\text{sens}} = [\mathbf{A}_{\text{sens}}, \mathbf{B}_{\text{sens}}, \mathbf{C}_{\text{sens}}, \mathbf{D}_{\text{sens}}]$ to provide the state space realization of the aeroelastic plant $\mathcal{S}_{\text{pl}}$ to be controlled. In this work, only ideal accelerometers that measure the accelerations in vertical direction are employed for the numerical realization of the sensor dynamics. The realization of such ideal sensors is provided by

$$\mathbf{a}_{z_i}(t) = \boldsymbol{\phi}_{\text{gh}}[z_i, :]\ddot{\mathbf{u}}_{\text{h}}(t) \tag{13}$$

where z_i denotes the index of the vertical DOF of point i. Further sensors might be selected for feedback including displacements, velocities, accelerations, grid point forces, and sectional loads.

3 CONTROL DESIGN METHODOLOGY

The aeroelastic plants generated as described in Section 2.2 are now employed for the synthesis of flutter suppression controllers. The control strategy employed in this manuscript is based on a simplified version of the $\mathcal{H}_\infty$-control framework for modal damping attenuation presented by Theis et al. [32]. This framework enables to augment the damping of critical flutter modes, while providing robustness against model uncertainty. Robustness is a key concern in this manuscript to ensure that the controller works also in the fully nonlinear environment described in Section 4. This $\mathcal{H}_\infty$ framework tackles the flutter suppression problem considering

the generalized CL shown in Fig. 2 where $\mathbf{K}(s)$ represents the generic LTI controller that elaborates the sensor measurements $\mathbf{y} \in \mathbb{R}^{n_y}$ and feed them back as a commanded control surface deflections $\boldsymbol{\delta_c} \in \mathbb{R}^{n_u}$, whereas $\mathbf{W}_e(s)$, $\mathbf{W}_u(s)$, and $\mathbf{W}_z(s)$ are weighting filters to be tuned for mixed-sensitivity loop shaping. The performance output $\mathbf{z} \in \mathbb{R}^{n_z}$ depends on the specific control objective.

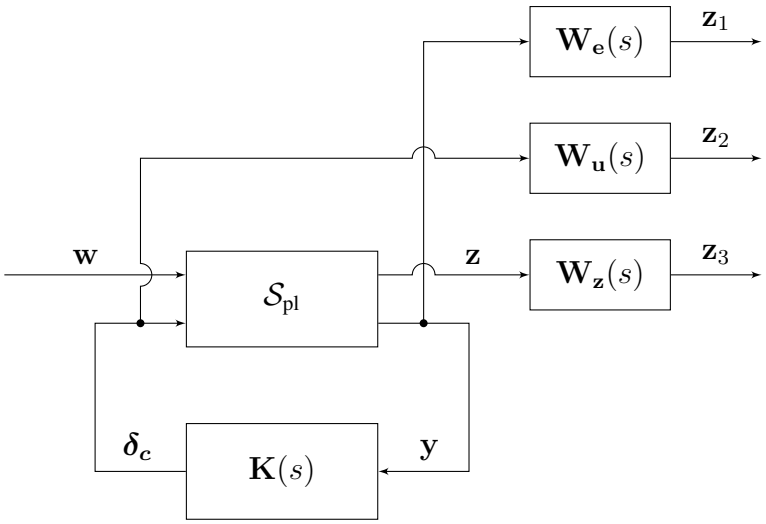

Figure 2: Illustration of the generalized closed-loop architecture for control design.

In this work, given an aeroelastic plant $\mathcal{S}_{\text{pl}}$ operating under a specific flow condition $\mathbf{p}_{\text{test}}$, chosen to correspond to a flutter point, the design objective is to find a LTI controller $\mathbf{K}(s)$ that accomplishes the following:

1. *Performance requirement:* stabilizes the aeroelastic plant $\mathcal{S}_{\text{pl}}$ at $\mathbf{p}_{\text{test}}$
2. *Robustness requirement:* ensure robustness with respect to modelling errors and neglected dynamics
3. Rejects the disturbance $\mathbf{w}$ entering at the plant input
4. Posses roll-off characteristics to avoid high frequency modes excitation and noise amplification
5. Preserves the low-frequency behaviour of the aeroelastic plant to avoid deflection of the control surfaces in steady-state
6. Generates control actions that remain within the saturation limits of the actuators.

Specifically, the CL system is considered stable when multi-input disk margins of $6\ \mathrm{dB}|45\ \mathrm{deg}$ are satisfied. These margins are also an additional metric for robustness verification. It is to be noted that the problem is framed as a regulation problem, where tracking capabilities are irrelevant and the output $\mathbf{y}$ serves as an error signal. Deterioration of stability for flow conditions that are already stable is here not required to facilitate the synthesis of $\mathbf{K}(s)$ and the illustration of the proposed workflow.

The performance requirement is fulfilled assuming the modal velocity of the flutter modes $\dot{\boldsymbol{\xi}}$ as the performance output $\mathbf{z}$ and penalizing the $\mathcal{H}_\infty$-norm of the transfer function between $\mathbf{w}$ and $\mathbf{z}_3 = \mathbf{W}_z(s)\dot{\boldsymbol{\xi}}$. This approach directly increases damping of the flutter modes as already demonstrated in the literature [24, 32]. Since the modal velocities $\dot{\boldsymbol{\xi}}$ already targets the specific narrow frequency range of the aeroelastic modes, $\mathbf{W}_z(s)$ is selected as a diagonal static gain such that $\dot{\boldsymbol{\xi}}$ is normalized to a magnitude of one. The weighting filter $\mathbf{W}_e(s)$ affects the rela-

tionship $\mathbf{z}_1 = \mathbf{W}_e\mathbf{H}_{yw}(s)\mathbf{S}(s)\mathbf{w}$, thus shaping the disturbance sensitivity $\mathbf{H}_{yw}(s)\mathbf{S}(s)$, where $\mathbf{S}(s) = (\mathbf{I} - \mathbf{K}(s)\mathbf{H}_{yw}(s))^{-1}$ is the input sensitivity of $\mathcal{S}_{\text{pl}}$ and $\mathbf{H}_{yw}(s)$ denotes its transfer function from $\mathbf{w}$ to $\mathbf{y}$, namely $\mathbf{y}(s) = \mathbf{H}_{yw}(s)\mathbf{w}(s)$. Since a peak sensitivity of less than two implies a gain margin of at least 6 dB [33], $\mathbf{W}_e(s)$ is selected as a static gain of the form $\mathbf{W}_e(s) = \text{diag}\left(W_{e,1}, W_{e,2}, \ldots, W_{e,n_z}\right)$ with $W_{e,i} \leq 0.5$ to limit sensitivity degradation to a factor of two. The weighting filter $\mathbf{W}_u(s)$ distributes control authority across the frequency. It is taken as a diagonal matrix with single elements parametrized as

$$W_{u,i} = V_{u,i}\left(\frac{s+\omega_{L,i}}{s+0.01\omega_{L,i}}\right)^2\left(\frac{s+\omega_{U,i}}{0.01s+\omega_{U,i}}\right)^2 \tag{14}$$

to confine the control activity of the i^{th} input in the frequency range between $\omega_{L,i}$ and $\omega_{U,i}$, whereas the value of $V_{u,i}$ bounds the maximum controller gain. With this parametrization, tuning is mainly performed through the static weights $W_{e,1}$ and $V_{u,i}$ as the values of $\omega_{L,i}$ and $\omega_{U,i}$ are imposed by the bandwidth requirements and require only minor modifications. Section 5 details the application of this controller to achieve stabilization of the BACT wing beyond the flutter threshold across various Mach numbers.

4 NONLINEAR CFD-CSM-AFS COUPLING PROCEDURE

To evaluate robustness of the controller with respect to model variations and unmodelled dynamics, a verification in a simulation environment that includes actuator and aerodynamic nonlinearities is carried out. The environment is built upon the PyCSM software [22], which has been enhanced to incorporate actuator dynamics and a mesh deformation module for implementing flap deflections based on the aileron deflections provided by the actuators $\boldsymbol{\delta}(t)$, thereby evolving the software into a new version termed PyCSM-ASE. The PyCSM-ASE workflow is illustrated in Figure 3. Note that the structure depicted in Figure 3 closely resembles that of Figure 1. Specifically, PyCSM-ASE operates based on a sequential logic and for each time step the following operations are carried out until the pre-defined simulation time is reached:

1. (**Only at $\mathbf{t} = \mathbf{0}$**) The initial state of the ASE simulation is set to that of a pre-computed trim state.
2. A disturbance in the form of a direct mode excitation of the FE model is introduced.
3. PyCSM (light blue box in Figure 3) simulates the system aeroelastic response to the input by calculating modal accelerations for each structural mode and the overall pressure field on the wet surface.
4. The computed data are elaborated by the sensors block that provides the new measurements $\mathbf{y}$ to be used for feedback. In this study, the sensors block receives only modal accelerations that are converted into physical measurements according to Eq. 13.
5. The $\mathcal{H}_\infty$ controller reads the physical acceleration history and generates the new commanded control surface deflections $\boldsymbol{\delta}_{\text{c}}$, which are processed by the actuators' dynamics to generate the new deflection angles $\boldsymbol{\delta}$.
6. The mesh module deforms the mesh based on the new control surface deflection $\boldsymbol{\delta}$, thus preparing the data for the successive time steps.

Note that the computation of $\mathbf{Q}_{\text{hh}}$ and $\mathbf{Q}_{\text{hc}}$, as detailed in Section 2.1, solely pertains to unsteady aerodynamic calculations. Therefore, only the CFD and the mesh deformation modules are necessary to perform these computations.

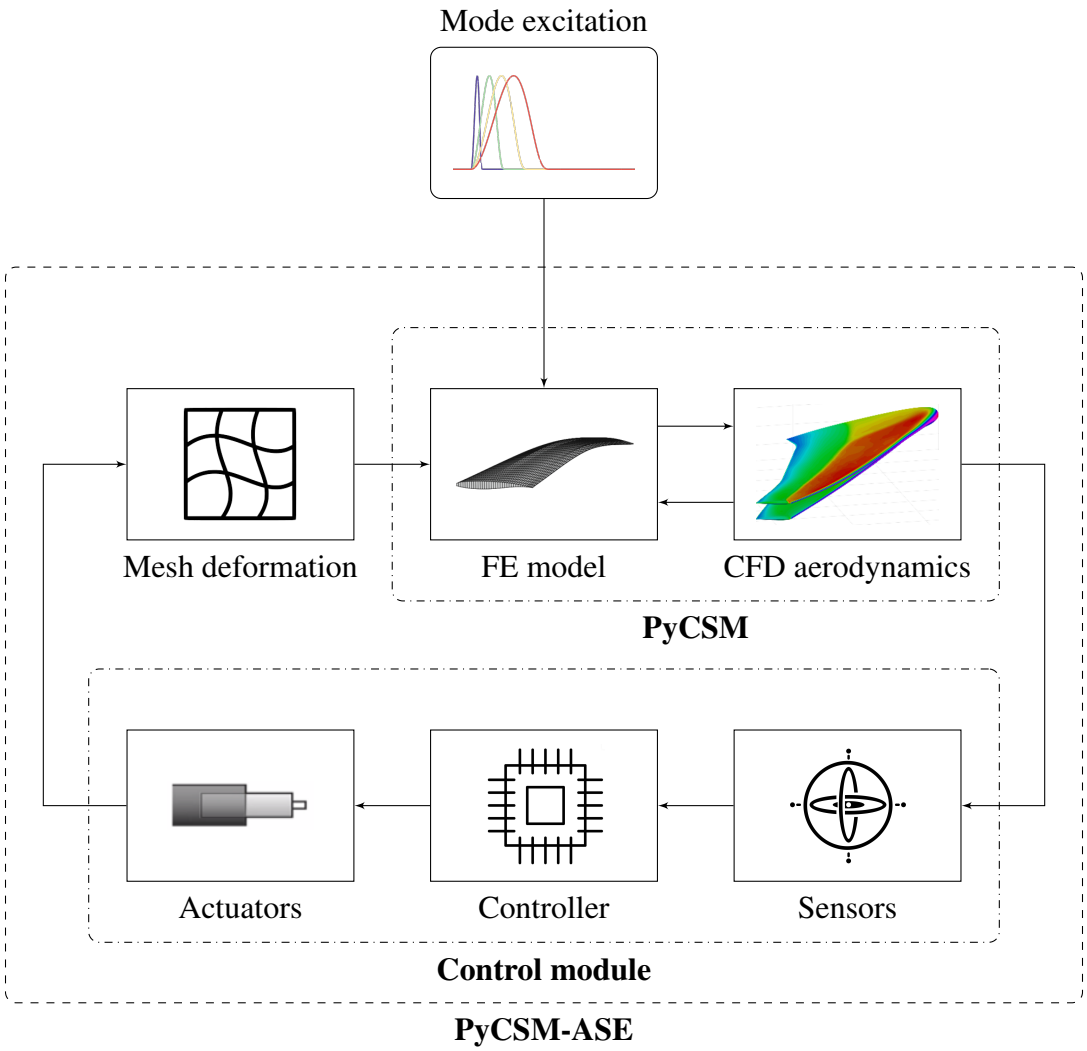

Figure 3: Block diagram of the PyCSM-ASE software for nonlinear aeroservoelastic simulation.

5 NUMERICAL MODEL AND RESULTS

5.1 The BACT model

The aeroelastic benchmark employed to illustrate the proposed workflow is the NASA BACT wing that was conceived to validate ASE computational models and at demonstrating flutter suppression in transonic regime [8–10]. The model consists of a rigid rectangular straight wing with a NACA 0012 airfoil section that is immersed in the air flow of the NASA Langley Transonic Dynamics Tunnel (TDT) [34]. The wing is mounted to a device called the Pitch and Plunge Apparatus (PAPA) which permits vertical translation (plunge motion) and rotation around the wing axis (pitch motion). Four accelerometers located at each corner of the wing measure accelerations in the plunge direction and are used for feedback, namely $\mathbf{y} = \{a_{\text{lei}}, a_{\text{tei}}, a_{\text{leo}}, a_{\text{teo}}\}$ where the subscripts denotes the sensor location as illustrated in Fig. 4, whereas the control action for flutter suppression is realized by a trailing edge flap actuated through an hydraulic actuator.

Based on the numerical data provided by Waszak [35], a Nastran FE model is generated to compute $\mathbf{K}_{\text{hh}}, \mathbf{C}_{\text{hh}}, \mathbf{M}_{\text{hh}}, \mathbf{M}_{\text{hc}}$, as well as the modal matrix $\boldsymbol{\phi}_{\text{gh}}$, which will be used as a modal basis for the generalization of the aerodynamic forces. The geometry of the wing is discretized by 800 aerodynamic panels for DLM computations as well as replicated with an unstructured

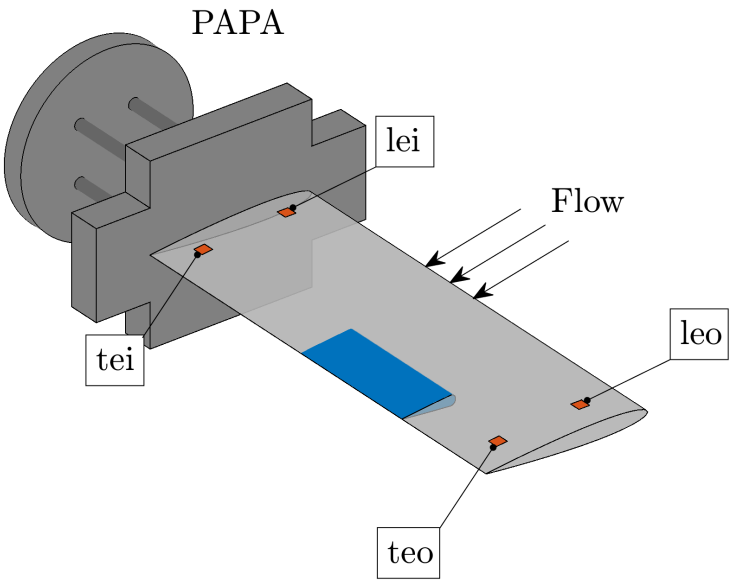

Figure 4: BACT wing representation with the PAPA mount as well as locations of the accelerometers ( ) and the trailing edge flap ( ) used for active flutter suppression.

mesh for CFD computations. The CFD mesh approximates the wet surface of the wing with 26.767 points and the farfield is modelled as a hemisphere closed by a symmetry plane. The DLM panneling along with the CFD mesh is depicted in Fig. 5. Furthermore, the model is

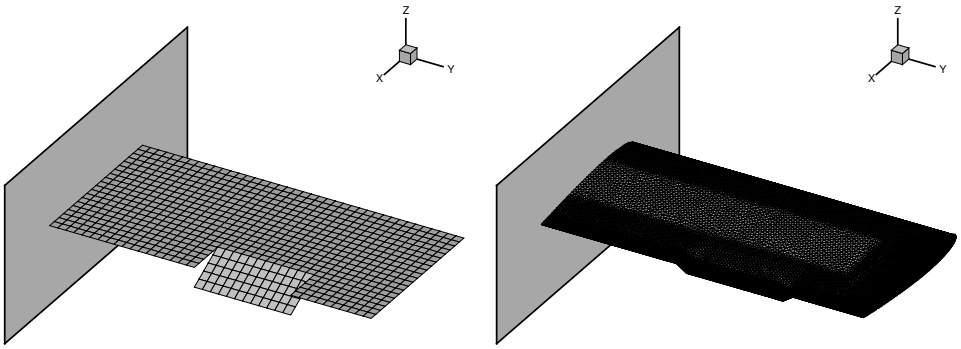

(a) DLM panels (b) CFD mesh

Figure 5: Aerodynamic models employed for the computation of the GAFs with deflected trailing edge flap.

augmented with the actuator dynamics of the 2^{nd} order identified in [35], whereas sensors are modelled adopting Eq.(13). The position limit for the trailing edge flap amounts to 12 deg, whereas the hydraulic actuators present rate saturation, but at values that are not in the range of interest. The perturbation term $\mathbf{f}_{\mathrm{h}}{}^{\mathrm{ext}}(t)$ is modelled as a pulse of the form of Eq. (7) and it impinges the pitch mode of the wing.

5.2 Unsteady aerodynamics

Unsteady aerodynamic loads are calculated for the BACT wing according to the methodology described in Section 2.1. While unsteady loads from DLM do not depend on the steady flow conditions, the procedure for the computation of Euler-based GAFs is affected by the angle of attack in trim state. In this case, the angle of attack is equivalent to the pitch angle, and its value

in steady-state is denoted as θ_0. In order to have a direct comparison all the CFD computations are carried out with $\theta_0 = 0\,\text{deg}$. Furthermore, the set of the dynamic pressure is adjusted to 80% of the flutter dynamic pressure q_{fl} at the specific Mach number. The selection of this value is only meant to ensure convergence of the CFD computations, but it does not affect the numerical values of $\mathbf{Q}_{\text{hh}}{}^{\text{Eul}}(ik, M_\infty, \rho_\infty, \text{geometry})$ and $\mathbf{Q}_{\text{hc}}{}^{\text{Eul}}(ik, M_\infty, \rho_\infty, \text{geometry})$.

GAFs are evaluated for a set of 31 reduced frequencies distributed in the frequency range $k = \left[0.001, 1.5\right]$ as well as seven Mach numbers equally spaced in the range $M_\infty = \left[0.4, 0.7\right]$. The terms of $\mathbf{Q}_{\text{hh}}(ik)$ and $\mathbf{Q}_{\text{hc}}(ik)$ that describe a moment contribution are given about the middle axis. The values of the GAFs are displayed only for the reference Mach numbers of 0.4 and 0.7 in Figs. 6 and 7, respectively, which represent slight and high compressible flow. The plots reveal a good correspondence between the calculated GAFs at $M_\infty = 0.4$, whereas discrepancies emerge notably at $M_\infty = 0.7$ as a result of the compressibility and geometrical effects that the DLM fails to capture.

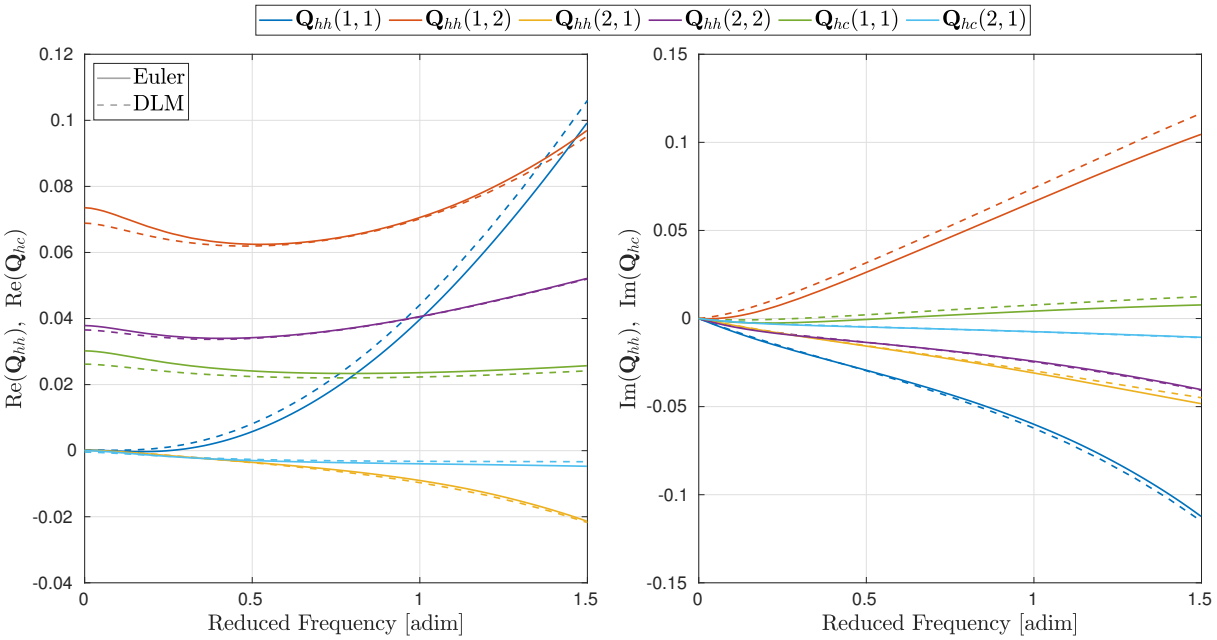

Figure 6: Calculated GAFs at Mach 0.4 (slight compressible flow).

5.3 Accuracy of Aeroelastic Plants

The GAFs presented in Section 5.2 are approximated through vector fitting routines. The achieved fitting is connected to the structural model according to Eq. (12), and the state space model is further augmented with actuators' and sensors' dynamics to obtain a representation of the aeroelastic plant in a state space form. Figures 8 and 9 show a comparison of the frequency response $\mathbf{H}_{y(1)u}(s) = \mathbf{H}_{a_{\text{lei}}u}(s)$ of the so-derived linear system at 80% and 120% of the flutter dynamic pressure for each specific Mach number. Figure 9 clearly illustrates different responses at the unstable point, namely at $q_\infty = 1.2 \cdot q_{\text{fl}}$, across the pitch mode frequency range, specifically $25 - 30\,\text{rad/s}$. This discrepancy stems from the different pressure fields predicted by the two unsteady aerodynamic methods. To clarify this point, Fig. 10 provides a comparison of the fields due to a sinusoidal flap excitation of $10\,\text{deg}$ and $\omega = 27\,\text{rad/s}$ at $q_\infty = 0.8 \cdot q_{\text{fl}}$ and $M_\infty = 0.70$[3]. It is evident from the arrows that the flap deflection generates a higher lift

[3]The incremental pressure distribution from DLM was computed by fitting the half-generalized aerodynamic forces $\mathbf{Q}_{\text{jh}}$ instead of $\mathbf{Q}_{\text{hh}}$. This approach, not essential for flutter computations, was already proposed by Kier and

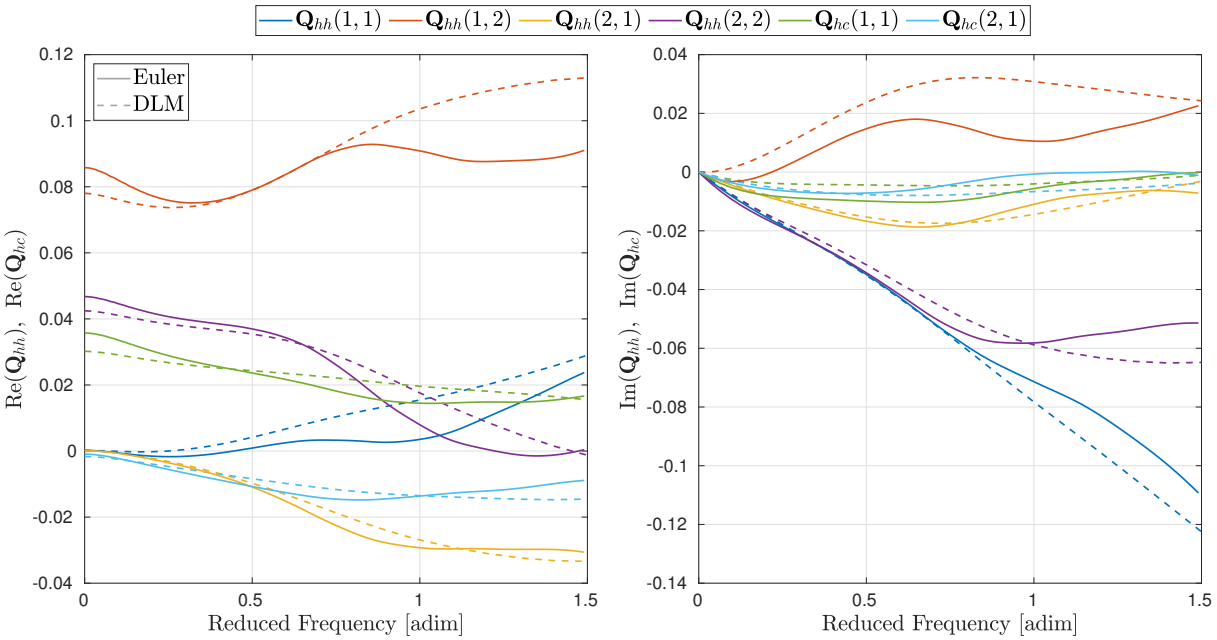

Figure 7: Calculated GAFs at Mach 0.7 (high compressible flow).

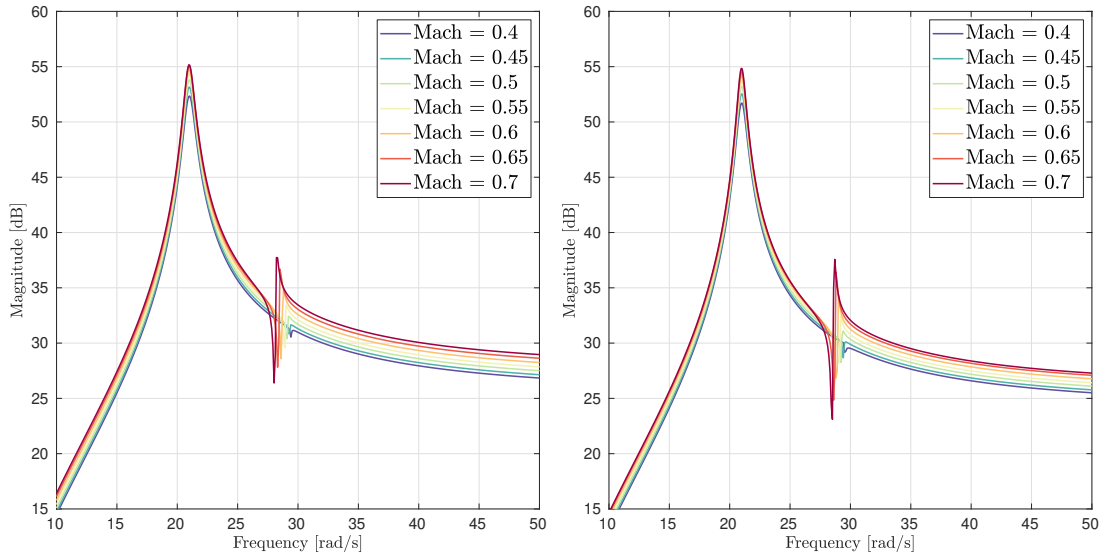

(a) Euler-based (b) DLM-based

Figure 8: Magnitude of the transfer function between δ_c and a_{leo} at $q_\infty = 0.8 \cdot q_{\text{fl}}$.

distribution according to Euler CFD, whereas DLM predicts a higher moment. Consequently, the wing exhibits a higher pitching tendency according to DLM, with the pitch contribution $\ddot{\theta}$ playing a more significant role than the plunge contribution $\ddot{h}$ for the LEO sensor. Therefore, the frequency response from DLM is higher at $w = 27\mathrm{rad/s}$, occurring just after the second peak in the frequency response. At higher dynamic pressures, this effect becomes more pronounced, leading to more evident differences as illustrated in Fig. 9. Conversely, for excitation frequencies preceding the peak, the situation is reversed.

In order to quantify the accuracy of the linear models, a reference response $\mathbf{H}_{\text{ref}}(\omega)$ is derived commanding the flap of the wing in PyCSM-ASE with sinusoidal inputs of varying frequencies

Looye [36]. CFD results are sourced directly from PyCSM-ASE.

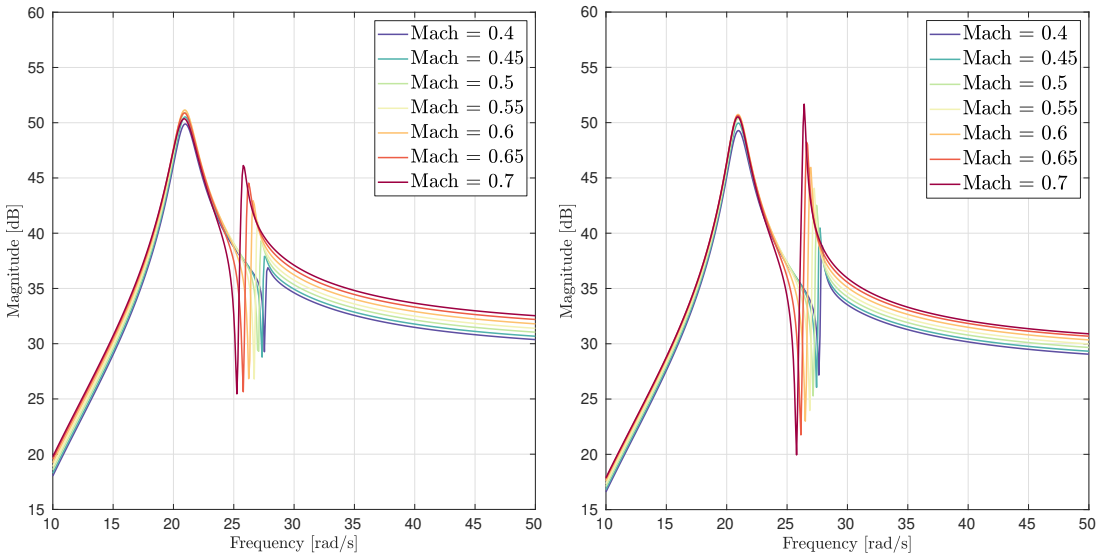

(a) Euler-based (b) DLM-based

Figure 9: Magnitude of the transfer function between δ_c and a_{leo} at $q_\infty = 1.2 \cdot q_{\text{fl}}$.

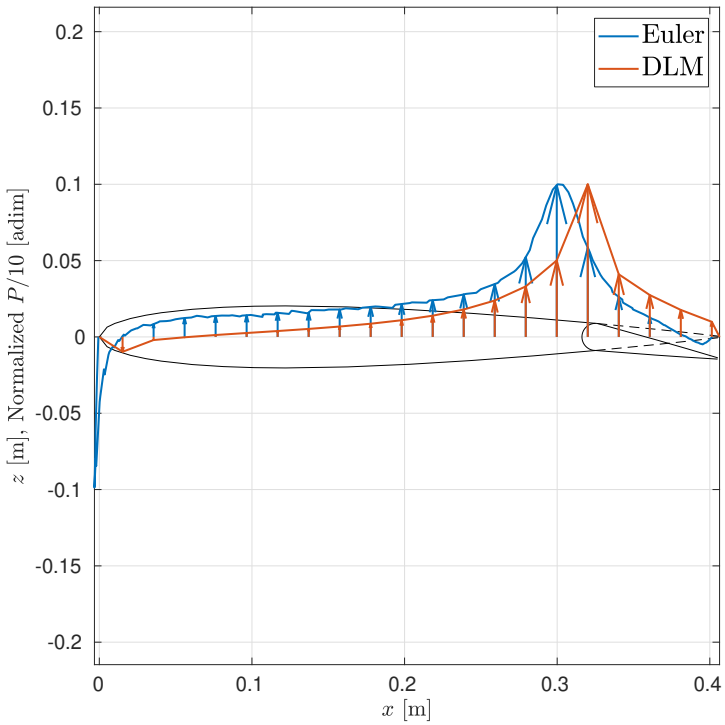

Figure 10: Incremental pressure field $P(\mathbf{x})$ due to a sinusoidal aileron deflection of 10 deg at $q_\infty = 0.8 q_{\text{fl}}$ and $M_\infty = 0.70$. The pressures are normalized to 0.1.

and the OL responses were computed for each excitation applying Eq. (8) between δ_c and the computed acceleration values. Figure 11 shows a direct comparison between the transfer response of the linear models and the high fidelity baseline from PyCSM-ASE at Mach number $M_\infty = 0.70$. The approximation error of the LTI models is computed as

$$\text{Relative error} = \frac{\|\mathbf{H}_{\text{ref}}(\omega)\| - \|\mathbf{H}_{\text{LTI}}(\omega)\|}{\|\mathbf{H}_{\text{ref}}(\omega)\|} \tag{15}$$

where $\mathbf{H}_{\text{LTI}}(\omega)$ denotes the response of the LTI models derived either from DLM or Euler-CFD.

The resulting errors are shown in Fig. 12 for the considered Mach numbers. Given that the

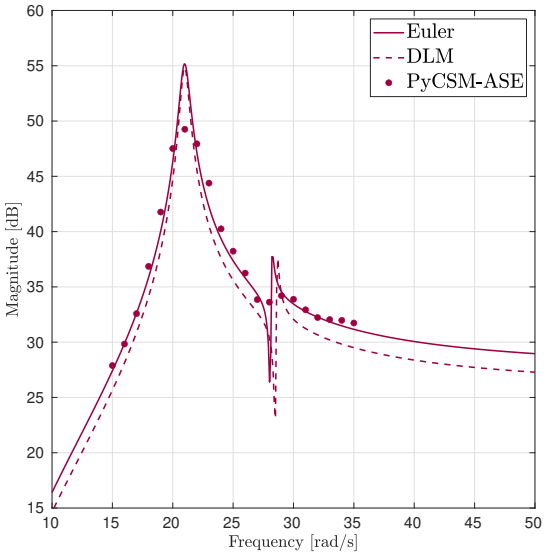

Figure 11: Transfer response of Fig.8 at $M_\infty = 0.7$ including PyCSM-ASE comparison.

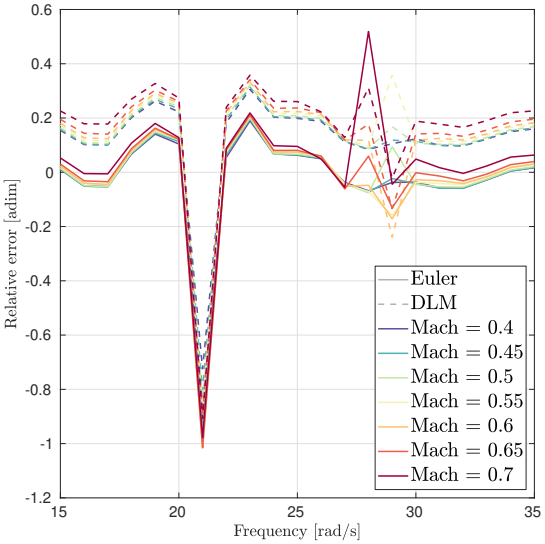

Figure 12: Relative error between linear models and PyCSM-ASE results.

state space models derived from Euler CFD were intended to capture more of the nonlinear effects than the DLM, the results derived from them were expected to align more closely with the higher-fidelity results from PyCSM-ASE. However, this is not as evident as expected. The Euler-based models appear to perform generally better at all the Mach numbers at frequencies in the $23 - 26$ rad/s range, in the low frequency range, i.e. $\omega \leq 20$ rad/s, and in the high frequency range i.e. $\omega \geq 30$ rad/s. These intervals do not cover the frequency range where the system exhibits peaks in its frequency response, which is where the two aeroelastic poles of the configuration lie. It can be seen that neither the Euler-based model nor the DLM-based model is able to properly capture the magnitude of the first peak of the response. In the region of the second peak, where the frequency response changes abruptly, no conclusions can be drawn, as the accuracy of the model depends on the specific frequency and Mach number selected. Furthermore, these trends cannot be extended to the response at $q_\infty = 1.2 \cdot q_{\text{fl}}$, where the state space models exhibit greater differences, and a comparison with PyCSM-ASE results is not possible due to the challenges in computing a diverging response over a sufficient time frame using CFD. Based on the above considerations, it is not possible to conclude that the Euler-based state space modes clearly outperform the DLM-based in the compressible flow regime.

5.4 Control Synthesis and Nonlinear Simulations

To demonstrate AFS, the system is considered at the specific flow conditions

$$\begin{aligned} \mathbf{p}_{\text{test}}(1) =& (M_\infty, q_\infty) = (0.4, 8.3\ \text{kPa}) \\ \mathbf{p}_{\text{test}}(4) =& (M_\infty, q_\infty) = (0.7, 8.9\ \text{kPa}) \end{aligned} \tag{16}$$

where the value of the dynamic pressures corresponds to 120% of q_{fl} for the respective Mach number. The generalized velocity $\dot{\boldsymbol{\xi}}$ of the flutter mode is added as a performance output $\mathbf{z}$. The frequency response from $\mathbf{f}_{\text{ext}}(t)$ to $\dot{\boldsymbol{\xi}}$, namely $\mathbf{H}_{\text{zw}}(i\omega)$, is depicted in Fig. 13 Based on the displayed response, it is decided to restrict control authority in the frequency range of $(\omega_L, \omega_U) = (15, 125)$ rad/s at $\mathbf{p}_{\text{test}}(1)$ and $(\omega_L, \omega_U) = (10, 125)$ rad/s at $\mathbf{p}_{\text{test}}(2)$. The value of ω_L is adjusted to cope with the frequency shift observed at the peak of $\mathbf{H}_{\text{zw}}(i\omega)$, while $\omega_U = 125$ rad/s represents a fraction of the actuator bandwidth and it is here assumed as the

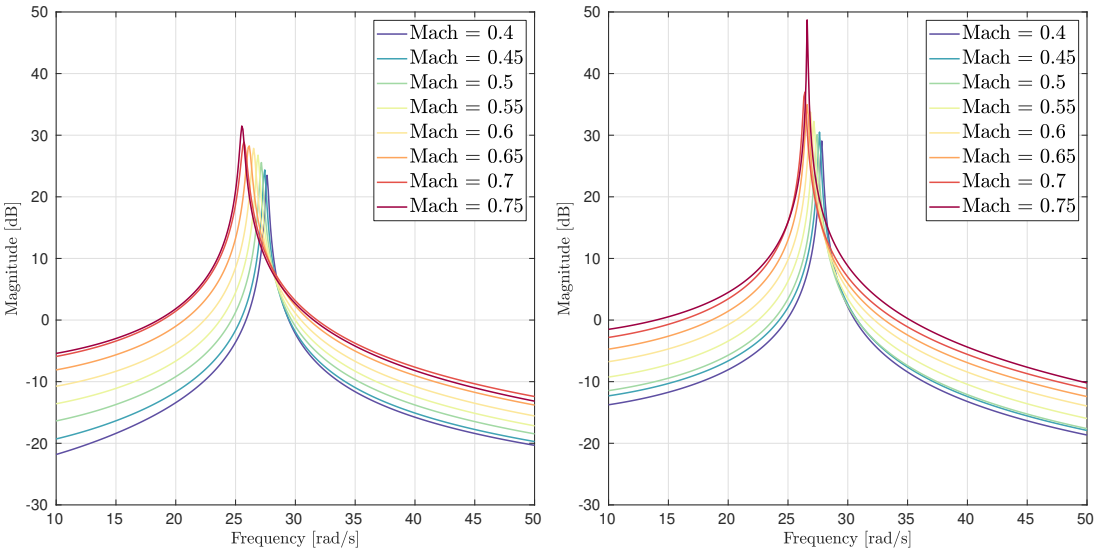

(a) CFD (b) DLM

Figure 13: Magnitude of the transfer function between $\mathbf{f}_{\text{ext}}(2)$ and $\dot{\boldsymbol{\xi}}$ at $q_\infty = 1.2 \cdot q_{\text{fl}}$.

available bandwidth of the CL system. The values of $W_{e,i}$ and V_u are adjusted based on the flow condition to ensure that both the Euler and DLM-based models meet the multi-input disk margin requirement outlined in Section 3. Specifically, the weight values remain constant during the controller synthesis for a given flow condition, allowing for comparability between the Euler and DLM-based controllers. Given the values of ω_L, ω_U, $W_{e,i}$, and V_u, MATLAB® hinfsyn routine was employed to synthesize the here presented controllers.

Differences between the Euler and DLM-based controllers become more apparent at this stage. The damping augmentation achieved through the synthesized controllers is depicted by the reduction of $\|\mathbf{H}_{\text{zw}}(s)\|_\infty$ compared to its open-loop (OL) value in Fig. 14. The sharp peak in

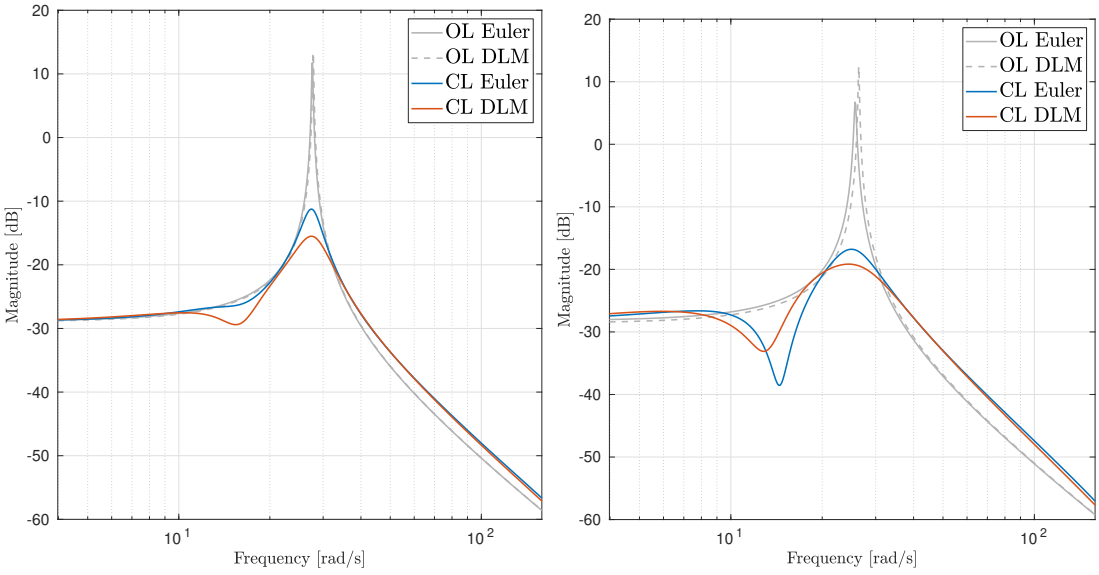

(a) $M_\infty = 0.40$ (b) $M_\infty = 0.70$

Figure 14: Magnitude of the transfer function between $\mathbf{f}_{\text{ext}}(2)$ and $\dot{\boldsymbol{\xi}}$ at $q_\infty = 1.2 \cdot q_{\text{fl}}$.

$\mathbf{H}_{zw}(i\omega)$ is reduced more when the aeroelastic plant based on DLM is employed. This is because the trailing edge flap is more efficient in altering the dynamics of the wing, as displayed by the transfer functions depicted in Fig. 9.

In order to evaluate the real performance of each controller, they are implemented in PyCSM-ASE, and the response of the resulting CL systems are simulated according to the workflow described in Section 4. The Euler solver implemented in the TAU code was employed for the simulation of unsteady aerodynamic effects. For comparison purposes, both the Euler-based and DLM-based plants are augmented with their respective controller and the resulting CL plants are simulated in a linear framework by means of the LSIM-H algorithm [37]. The time responses displayed in Fig. 15 and Fig. 16 correspond to a unit pulse excitation of the pitch mode, which impacts the system at $\tau = 0.04$ s. The steady-state pitch angle of the wing is set to $\theta_0 = 0$ deg. While both controllers effectively stabilize the system, it is evident from the

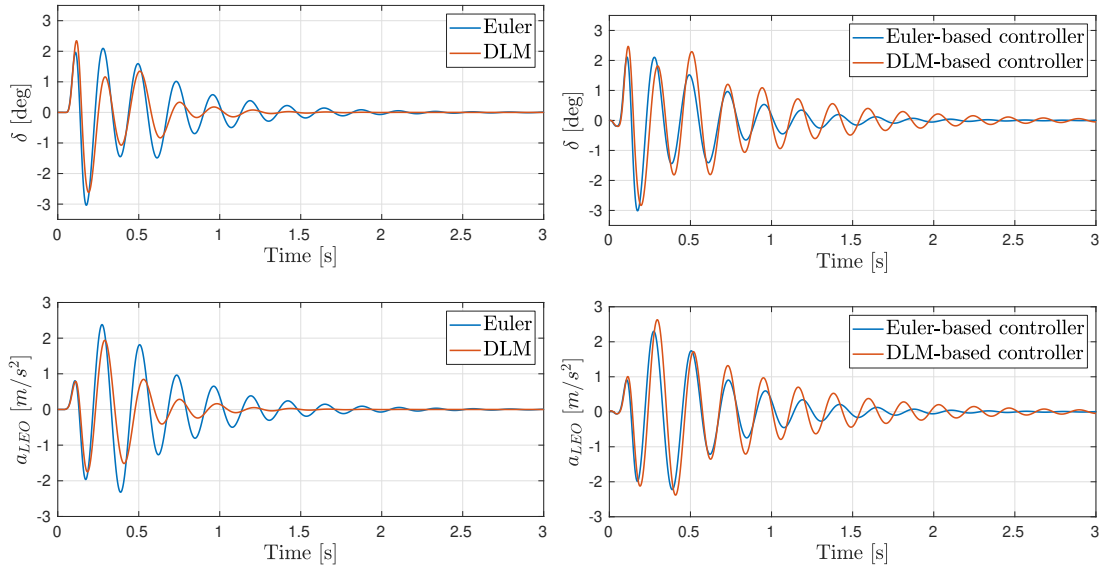

(a) Linear results from LSIM-H (b) Nonlinear results from PyCSM-ASE

Figure 15: Time response of the CL system at $\mathbf{p}_{\text{test}}(1)$ due to a unit pulse $\mathbf{f}_{\text{h}}^{\text{ext}}(2)$ of the form of Eq. (7) with $t_0 = 0.1$ s, delay $\tau = 0.04$ s, and $\theta_0 = 0$ deg.

nonlinear results shown in Fig. 15(b) and Fig.16(b) that the Euler-based controller outperforms the DLM-based, as the rate of acceleration decay in the former is faster. This is contradictory to the linear results displayed in Figs. 15(a) and 16(a), which are consistent with the magnitude of $\mathbf{H}_{zw}(s)$ shown in Fig. 14. This is presumably because of the Euler-based plant ability to capture nonlinear aerodynamics that are beyond the DLM ability to predict. Furthermore, the nonlinearities that are present at the selected flow conditions with the wing at null pitch angle in steady-state are not strong enough to affect the stability of the CL system.

Figure 17 displays results of nonlinear simulations for varying steady-state pitch angle at $\mathbf{p}_{\text{test}}(2)$. A perturbation of the initial state can be considered as the effect of atmospheric perturbations or wind tunnel turbulence. In these simulations, saturation on $|\delta(t)|$ is intentionally deactivated to concentrate on the effects of nonlinear aerodynamics. While the Euler-based controller can withstand the external perturbation for both $\theta_0 = 0.5$ deg and $\theta_0 = 0.75$ deg, the DLM-based controller leads to significantly high flap deflections for $\theta_0 = 0.75$ deg, resulting in a lack of convergence in the unsteady aerodynamic solver. Therefore, stability cannot be guaranteed. This analysis proves that the CFD-based controller also is more robust than the DLM-based

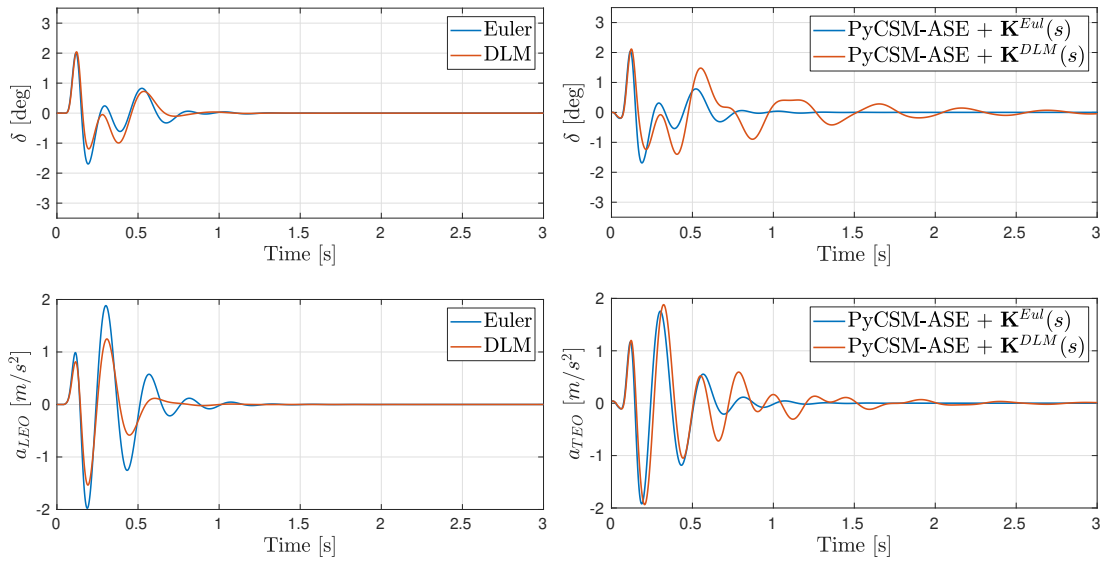

(a) Linear results from LSIM-H (b) Nonlinear results from PyCSM-ASE

Figure 16: Time response of the CL system at $\mathbf{p}_{\text{test}}(2)$ due to a unit pulse $\mathbf{f}_{\text{h}}^{\text{ext}}(2)$ of the form of Eq. (7) with $t_0 = 0.1$ s, delay $\tau = 0.04$ s, and $\theta_0 = 0$ deg.

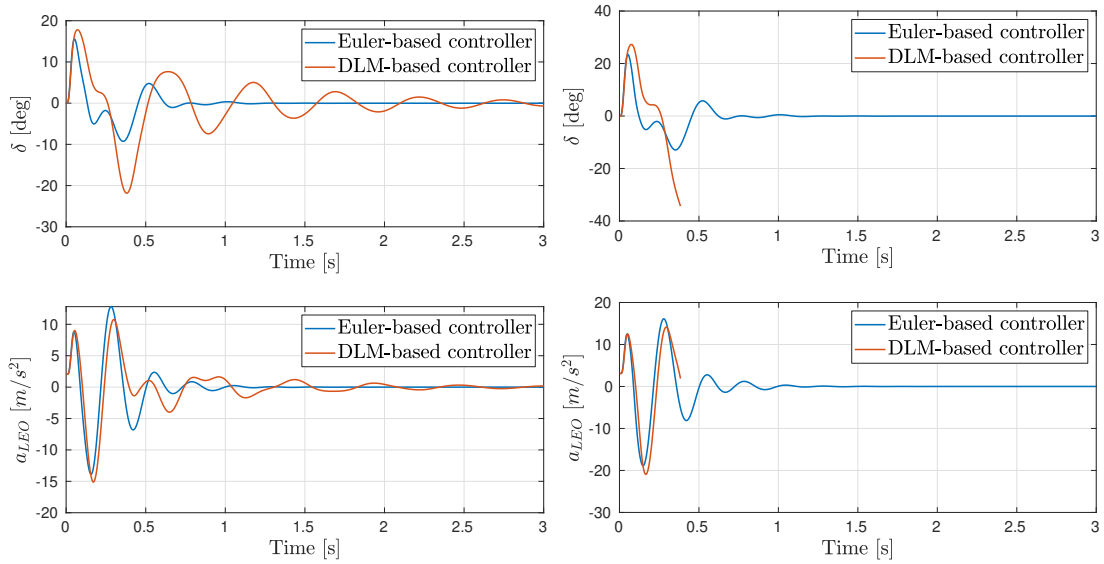

(a) $\theta_0 = 0.5$ deg (b) $\theta_0 = 0.75$ deg

Figure 17: Time response of the CL system at $\mathbf{p}_{\text{test}}(2)$ due to a unit pulse $\mathbf{f}_{\text{h}}^{\text{ext}}(2)$ of the form of Eq. (7) with $t_0 = 0.1$ s, delay $\tau = 0.04$ s, and varying θ_0. Results are obtained using PyCSM-ASE.

controller to external perturbations [24, 38, 39].

6 CONCLUSIONS AND FUTURE WORK

In this paper, we have presented a complete end-to-end workflow ranging from the construction of LTI aeroelastic models with aerodynamics based on Euler CFD up to the post-synthesis verification of AFS feasibility in a nonlinear simulation environment (PyCSM-ASE). The workflow is illustrated using the BACT wing, an aeroelastic benchmark from NASA for ASE activities. Since this benchmark is representative of a generic wind-tunnel configuration and data used are in standard format, the methodologies illustrated are applicable to real-life wind-tunnel prob-

lems.

Specifically, GAFs were derived from Euler-CFD and compared with DLM GAFs showing a good agreement of the results in the low subsonic region, whereas discrepancies arise with increasing Mach number due to compressibility effects. LTI models in a state space form were constructed by approximating both the Euler and DLM GAFs using vector fitting routines. A comparison of the frequency response of the resulting state space models with the results derived from PyCSM-ASE did not indicate superior performance of one LTI realization over the other. The state space realizations were further employed to synthesize $\mathcal{H}_\infty$ controllers aiming at AFS, and the CL systems were simulated both in a linear and a nonlinear ASE environment. At this stage, the nonlinear simulations clearly show that the Euler-based controller outperforms the DLM-based controller in terms of both performance and robustness. Remarkably, the linear simulations predict an opposite trend, highlighting the importance of conducting post-synthesis verification in an appropriate nonlinear ASE environment.

Future directions of research include (i) analyses of the system at higher Mach numbers where nonlinearities typical of transonic flows might more strongly influence the solution, (ii) enhancing the synthesis to ensure the functionality of the controller over a large range of flow conditions, and (iii) further developing PyCSM-ASE to include noise measurements and delays in the closed-loop. The use of RANS-based GAFs is also envisaged.

7 REFERENCES

[1] Theodorsen, T. (1949). General theory of aerodynamic instability and the mechanism of flutter. Tech. Rep. TR-496, NACA.

[2] (2023). Federal aviation regulations part 25: Airworthiness standards: Transport category airplanes. Tech. Rep. Tech. Rep. FAA Regulation No. 13, Federal Aviation Administration.

[3] (2019). Certification Specifications and Acceptable Means of Compliance for Large Aeroplanes. Tech. Rep. CS-25 Amd. 16, European Aviation Safety Agency.

[4] Livne, E. (2018). Aircraft active flutter suppression: State of the art and technology maturation needs. *Journal of Aircraft*, 55(1), 410–452. doi:10.2514/1.C034442.

[5] ALBANO, E. and RODDEN, W. P. (1969). Errata: "doublet-lattice method for calculating lift distributions on oscillating surfaces in subsonic flows". *AIAA Journal*, 7(11), 2192a–2192a. doi:10.2514/3.55530.

[6] KALMAN, T. P., RODDEN, W. P., and GIESING, J. P. (1971). Application of the doublet-lattice method to nonplanar configurations in subsonic flow. *Journal of Aircraft*, 8(6), 406–413. doi:10.2514/3.59117.

[7] Schildkamp, R., Chang, J., De Breuker, R., et al. (2022). Incremental nonlinear control for aeroelastic wing load alleviation and flutter suppression. In *International Forum on Aeroelasticity and Structural Dynamics (IFASD)*. Madrid, Spain.

[8] Mukhopadhyay, V. (2000). Benchmark active control technology: Part i. *Journal of Guidance, Control, and Dynamics*, 23(5), 913–913. doi:10.2514/2.4631.

[9] Mukhopadhyay, V. (2000). Benchmark active control technology special section: Part ii. *Journal of Guidance, Control, and Dynamics*, 23(6), 1093–1093. doi:10.2514/2.4659.

[10] Mukhopadhyay, V. (2001). Benchmark active control technology special section: Part iii. *Journal of Guidance, Control, and Dynamics*, 24(1), 146–146. doi:10.2514/2.4693.

[11] Fonte, F., de Gaspari, A., Riccobene, L., et al. (2019). Numerical and experimental investigations on active flutter suppression technologies. In *International Forum on Aeroelasticity and Structural Dynamics (IFASD)*. Savannah, Georgia, USA.

[12] Ricci, S., Marchetti, L., Riccobene, L., et al. (Jan 2021). An active flutter suppression (afs) project: Overview, results and lessons learned. *AIAA Scitech 2021 Forum 2021-0908*. doi: 10.2514/6.2021-0908.

[13] Mattaboni, M., Quaranta, G., and Mantegazza, P. (2009). Active flutter suppression for a three-surface transport aircraft by recurrent neural networks. *Journal of Guidance, Control, and Dynamics*, 32(4), 1295–1307. doi:10.2514/1.40774.

[14] Ricci, S., Toffol, F., De Gaspari, A., et al. (2022). Wind tunnel system for active flutter suppression research: Overview and insights. *AIAA Journal*, 60(12), 6692–6714. doi: 10.2514/1.J061985.

[15] Miller, C., Schaefer, J., Boucher, M., et al. (2022). X-56a flight-test approach for envelope expansion past open-loop flutter instability. Tech. Rep. STO-MP-SCI-328, NATO/OTAN.

[16] Schaefer, J., Suh, P., Boucher, M., et al. (2023). Flying beyond flutter with the x-56a aircraft. Tech. Rep. TM-20220012337, NASA.

[17] Takarics, B., Patartics, B., Luspay, T., et al. *Active Flutter Mitigation Testing on the FLEXOP Demonstrator Aircraft*. doi:10.2514/6.2020-1970.

[18] Fischer, A., Schröder, F., and Thormann, R. (2022). Active flutter suppression from an industrial perspective. In *International Forum on Aeroelasticity and Structural Dynamics (IFASD)*. Madrid, Spain.

[19] de Souza, A. D. R., Poussot-Vassal, C., Vuillemin, P., et al. (2023). Aircraft flutter suppression: from a parametric model to robust control. In *2023 European Control Conference (ECC)*. pp. 1–6. doi:10.23919/ECC57647.2023.10178141.

[20] Waite, J., Stanford, B., Bartels, R. E., et al. *Active Flutter Suppression Controllers Derived from Linear and Nonlinear Aerodynamics: Application to a Transport Aircraft Model*. doi: 10.2514/6.2018-2836.

[21] Grauer, J. A. and Waite, J. *Design of a Collocation-Based Active Flutter Suppression Control Law for the IAWTM Wind Tunnel Model*. doi:10.2514/6.2024-2201.

[22] Neumann, J. and Mai, H. (2013). Gust response: Simulation of an aeroelastic experiment by a fluid–structure interaction method. *Journal of Fluids and Structures*, 38, 290–302. ISSN 0889-9746. doi:https://doi.org/10.1016/j.jfluidstructs.2012.12.007.

[23] Schwamborn, D., Gerhold, T., and Heinrich, R. (2006). The dlr tau-code: Recent applications in research and industry. In *In Proceedings of the European Conference on Computational Fluid Dynamics (ECCOMAS)*.

[24] Micheli, B. (2024). Active flutter suppression: Quantification of performance loss due to actuator saturation. *Journal of Guidance, Control, and Dynamics (accepted for publication)*.

[25] Inc, Z. T. (1017). *ZAERO Theoretical Manual. Version 9.3.*

[26] Kaiser, C., Thormann, R., Dimitrov, D., et al. (2015). Time-linearized analysis of motion-induced and gust-induced airloads with the dlr tau code. In *Deutscher Luft- und Raumfahrtkongress 2015*.

[27] Beckert, A. and Wendland, H. (2001). Multivariate interpolation for fluid-structure-interaction problems using radial basis functions. *Aerospace Science and Technology*, 5(2), 125–134. doi:10.1016/S1270-9638(00)01087-7.

[28] Farhat, C. and Lesoinne, M. (2000). Improved staggered algorithms for the serial and parallel solution of three-dimensional non linear transient aeroelastic problems. *Computer Methods in Applied Mechanics and Engineering*, 182, 499–515. doi:10.1016/S0045-7825(99)00206-6.

[29] Gustavsen, B. and Semlyen, A. (1999). Rational approximation of frequency domain responses by vector fitting. *IEEE Transactions on Power Delivery*, 14(3), 1052–1061. doi:10.1109/61.772353.

[30] Gustavsen, B. (2006). Improving the pole relocating properties of vector fitting. *IEEE Transactions on Power Delivery*, 21(3), 1587–1592. doi:10.1109/TPWRD.2005.860281.

[31] Deschrijver, D., Mrozowski, M., Dhaene, T., et al. (2008). Macromodeling of multiport systems using a fast implementation of the vector fitting method. *IEEE Microwave and Wireless Components Letters*, 18(6), 383–385. doi:10.1109/LMWC.2008.922585.

[32] Theis, J., Pfifer, H., and Seiler, P. (2020). Robust modal damping control for active flutter suppression. *Journal of Guidance, Control, and Dynamics*, 43(6), 1056–1068. doi:10.2514/1.G004846.

[33] Skogestad, S. and Postlethwaite, I. (2005). *Multivariable Feedback Control: Analysis and Design*, vol. 2.

[34] Baals, D. and Corliss, W. (1981). Wind tunnels of nasa. Tech. rep., NASA SP-440.

[35] Waszak, M. (1998). Modeling the benchmark active control technology wind-tunnel model for active control design applications. Tech. Rep. NASA Tech. Rep. 1998-206270, Langley Research Center, NASA.

[36] Kier, T. and Looye, G. (2009). Unifying manoeuvre and gust loads analysis. In *IFASD 2009*.

[37] Jeličić, G., Böswald, M., and Brandt, A. (2021). Improved computation in terms of accuracy and speed of lti system response with arbitrary input. *Mechanical Systems and Signal Processing*, 150, 107252. ISSN 0888-3270. doi:https://doi.org/10.1016/j.ymssp.2020.107252.

[38] Goman, M., Patel, Y., and Sidoryuk, M. (August 2003). Regions of attraction for robustness assessment. *AIAA Guidance, Navigation, and Control Conference and Exhibit, AIAA Paper 2003–5551*. doi:10.2514/6.2003-5551.

[39] Micheli, B. (2022). Active flutter suppression of a two-dimensional airfoil with actuator saturation. In *International Forum on Aeroelasticity and Structural Dynamics (IFASD)*. Madrid, Spain.

COPYRIGHT STATEMENT